Materials Science & Engineering A 817 (2021) 141353

Contents lists available at ScienceDirect

Materials Science & Engineering A

journal homepage: www.elsevier.com/locate/msea

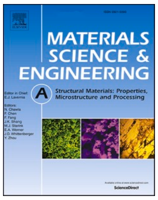

Stretch-flangeability correlated with hardness distribution and strain-hardenability of constituent phases in dual- and complex-phase steels

Eunji Song [a], Gun-Hee Lee [b], Hansol Jeon [a], Bong June Park [c,**], Jung-Gu Lee [b,***], Ju-Young Kim [a,*]

[a] *Department of Materials Science and Engineering, UNIST (Ulsan National Institute of Science and Technology), Ulsan, 44919, Republic of Korea*
[b] *School of Materials Science and Engineering, University of Ulsan, Ulsan, 44776, Republic of Korea*
[c] *Automotive Steel Products Design Team, Technical Research Center, Hyundai Steel, Chungcheongnam-do, 31719, Republic of Korea*

ARTICLE INFO

Keywords:
Nanoindentation
Dual-phase steels
Complex-phase steels
Formability
Strain-hardenability

ABSTRACT

Stretch-flangeability as a parameter of formability is measured on dual-phase (DP) and complex-phase (CP) steels by the hole-expansion ratio (HER), and nanoindentation is introduced to assess the hardness of constituent phases before and after HER testing. Hole-expansion ratios of two dual-phase (DP1, DP2) and one complex-phase (CP1) steels are measured as 51%, 126% and 136%, respectively. The primary site of void formation is found to be the interfacial boundary for DP1, the ferrite phase close to the martensite phase where numerous geometrically necessary dislocations (GNDs) are formed for DP2, and the martensite phase for CP1. The hardness ratio of the hard to soft phase is a key indicator of formability, and this introduces the stress concentration from strain disparity at the interfacial boundaries between the hard and soft phases. Here, it is founded that strain-hardenability of constituent phases depends on the hardness of the GND layer, and the strain disparity under deformation is determined by the GND layer hardness as well as the hardness ratio of the hard to soft phase. This study suggests the GND layer as a stress-dispersion layer and the hardness of GND layers in soft phases as a critical role in formability.

1. Introduction

Dual-phase (DP) steels composed of ferrite and martensite, and complex-phase (CP, also called tri-phase [1]) steels composed of ferrite, martensite, and bainite phases, are widely used as structural materials, especially in the automotive industry. Even though they have adequate strength and ductility simultaneously, their low local formability has been a critical issue. The strain disparity between constituent phases with different mechanical properties induces stress concentrations at interfacial boundaries that have been shown to be a primary cause of poor formability. Thus, understanding the mechanical properties of constituent phases is critical in designing and enhancing mechanical properties of DP and CP steels. Previous results for DP steels show that local strain develops more in soft ferrite phases than in hard martensite phases during tensile testing, resulting in a severe strain disparity between constituent phases [2–4]. Stress concentrations caused by this strain disparity assist the formation of voids at the interfacial boundaries, and this promotes nucleation and propagation of cracks along these boundaries [5]. Electron backscatter diffraction (EBSD) and X-ray microtomography have shown that the strain disparity is alleviated by increased tempering temperature, and the disparity in hardness of hard and soft phases has been suggested as a primary factor determining strain disparity and void formation at interfacial boundaries [4,6–8]. Nanomechanical tests have been used to investigate the mechanical properties of constituent phase at the sub-micron scale [9]. Uniaxial stress-strain curves of each phase in DP steels were measured by tension and compression of nanopillars prepared by focused ion-beam (FIB) milling [10,11]. These provided strengths and strain-hardening rates of constituent phases that, combined with computational simulations, were useful in predicting mechanical behavior and formability of the DP steels [12,13]. Recently, hardness measurements of constituent phases by nanoindentations revealed that narrower hardness distributions contribute to a decrease in stress concentration by strain disparity, and that introduction of phases with intermediate hardness such as bainite

---

** Corresponding author.
*** Corresponding author.
* Corresponding author.

E-mail addresses: bjpark79@hyundai-steel.com (B.J. Park), jglee88@ulsan.ac.kr (J.-G. Lee), juyoung@unist.ac.kr (J.-Y. Kim).

https://doi.org/10.1016/j.msea.2021.141353
Received 1 August 2020; Received in revised form 21 April 2021; Accepted 26 April 2021

Table 1
Chemical compositions of DP1, DP2, and CP1 steels (weight percent).

	C	Si + Al	Mn	Cr + Mo
DP1	0.12	1.1	2.2	0.5
DP2	0.16	1.6	2.2	0.1
CP1	0.12	0.3	2.2	0.5

and tempered martensite phases between hard and soft phases increases formability [14,15]. Also, it was observed that inhomogeneity of deformation in the ferrite phase increases with proximity to the martensite phase, where the geometrically necessary dislocations (GNDs) form by volume expansion of the martensite phase transformation (called the GND layer).

Here, GND layers in soft phases compared to the hard and soft phases are found to play a role in stress dispersion at interfacial boundaries and are thus related to formability. Stress concentration sites in DP and CP steels are investigated with void formation after hole-expansion ratio (HER) testing. Nanoindentation was performed on DP and CP steels before and after HER testing. The increase in hardness of the constituent phases and GND layer after HER testing indicates the strain hardenability of constituent phases under non-uniform strain distribution. These results suggest dependence of the strain hardenability of constituent phases on the hardness of the GND layer as well as on the hardness ratio between hard and soft phases.

2. Materials and methods

The steels were manufactured as 45-mm thick cast ingots by vacuum melting with chemical compositions as listed in Table 1. The ingots were heat-treated at 1250 °C for 2 h and hot-rolled to form a 3.2-mm thick plate by serial hot rolling 7 times at 900 °C. After the hot-rolling process,

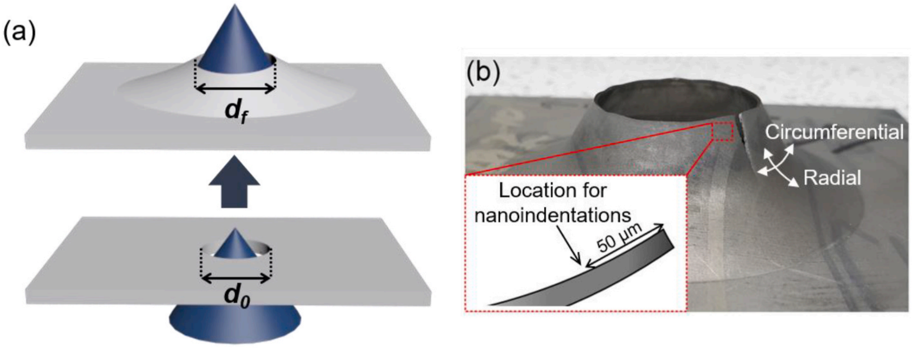

Fig. 1. (a) Schematic of hole expansion ratio (HER) test and (b) sample image after HER testing.

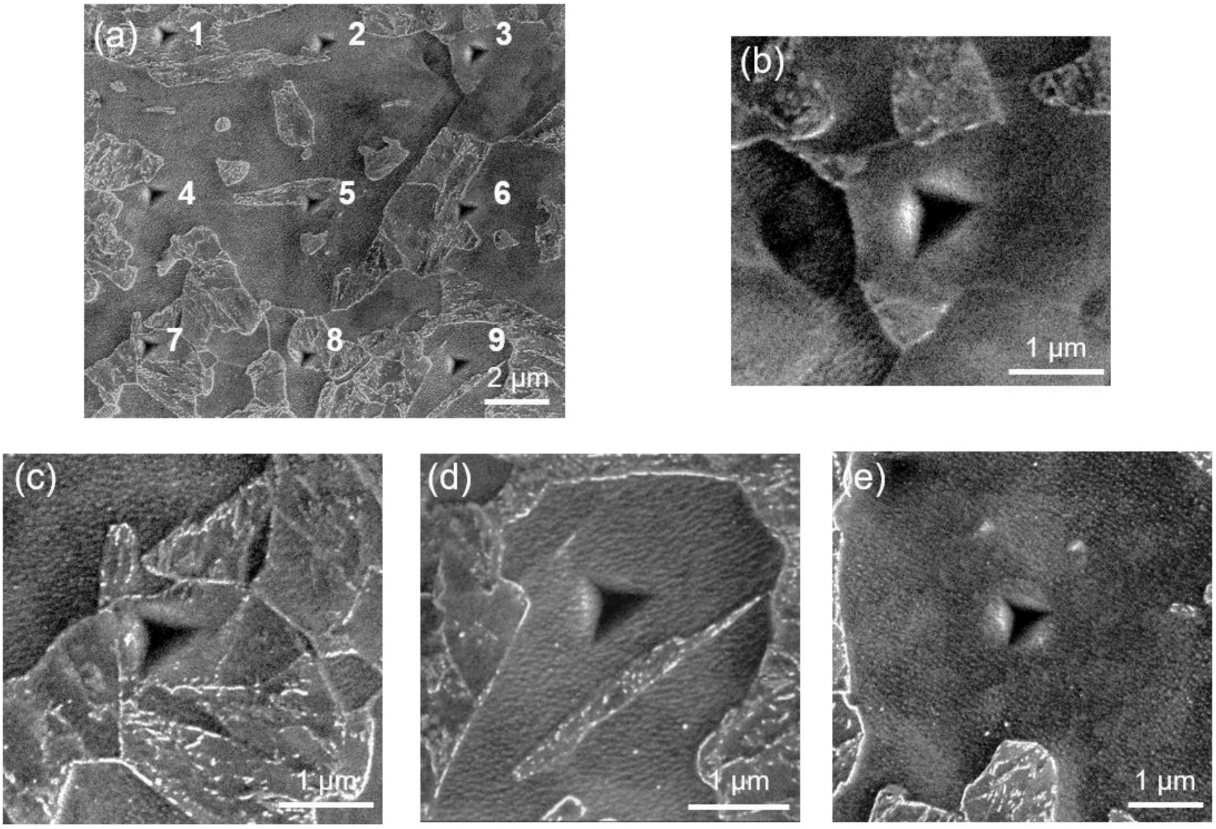

Fig. 2. SEM images showing (a) nanoindentation arrays, (b–d) detail of indents 3, 7, and 9 counted as indents on martensite, tempered martensite, ferrite phase close to tempered martensite phases, and (e) detail of indent on ferrite phase.

the plates were held at 550 °C for 2 h, followed by furnace cooling. An additional 6–8 serial cold-rollings were carried out to reduce the thicknesses of the plates by 50%, generating fine ferrite-pearlite structures.

Ferrite-austenite phases were obtained from the ferrite-pearlite structure with inter-critical heat treatment at 835 °C for 80 s. Cooling was performed down to the martensite start temperature M_s within 30 s, and in order to temper the martensite phases cooling was held at 320 °C for 240 s for DP steel and 385 °C for 240 s for CP steel (the lower cooling rate was chosen for CP steel in order to form bainite phases). Finally, DP steel samples composed of ferrite-martensite-tempered martensite, and CP steel samples composed of ferrite-martensite-tempered martensite-bainite phases, were prepared, called DP1 and CP1 hereafter. For comparison, one (called DP2 hereafter) was selected from commercially obtainable DP steels because DP2 has characteristics similar to CP1, including phase volume fraction, phase size, and hardness distribution. Specimens for HER tests and nanoindentation were extracted from the middle of the rolling and width direction of the bulk DP and CP steels. The top surfaces of specimens for nanoindentation were mechanically polished to reduce the thickness from 1.6 mm to 0.8 mm, so the nanoindentations were performed in the middle of the thickness direction.

HER tests were performed by inserting a conical tip through a hole in the steel plates and stopping as soon as a primary crack was introduced, as shown in Fig. 1a. For the HER tests, circular holes of diameter d_0 10 mm were machined in the middle of the plates by electric-discharge wire cutting. Unlike mechanical hole punching, electric-discharge wire cutting does not introduce severe shear deformation at the perimeter of holes [16,17], so that any increase in hardness is derived from strain hardening during HER testing. Microstructure observations and hardness measurements after HER testing were carried out at the upper surface of the hole edge near primary cracks (Fig. 1b), where the triaxial stress state amplifies the stress concentration by strain disparity predominantly at interfacial boundaries. All SEM images showing microstructure, void formation, and residual indentation marks were measured by FE-SEM (Quanta 3D FEG, FEI) in imaging mode of second electron (SE).

Nanoindentations were performed on DP and CP samples before and after HER testing. Nanoindentation samples were prepared by mechanical polishing using a diamond suspension with particle size 0.25 µm and electropolishing by 10% perchloric acid and 90% acetic acid. At least 200 nanoindentations were performed on each sample using a G200 nanoindenter with a Berkovich indenter in the CSM (continuous stiffness measurement) mode at indentation strain rate 0.05 s^{-1}. The maximum indentation depth was 100 nm and spacing between indents was 5 µm. All residual indentation marks were observed by FE-SEM (Quanta 3D FEG, FEI) to identify nanoindentation locations of grain interior and grain boundary. Nanoindentations formed on a grain/interfacial boundary, such as locations 2, 4, 5, 6, and 8 in Fig. 2a, were excluded to avoid the effect of grain boundaries or interfacial boundaries when analyzing hardness of constituent phases. Nanoindentations shown in Fig. 2(b–e) were classified into martensite, tempered martensite, GND layer, and ferrite phases, respectively. Hardness as well as microstructure for tempered martensite and bainite phases are found to be so similar that nanoindentations on bainite phases are considered to be tempered martensite phases in CP1.

Additionally, the hardness of GND layers that formed on ferrite phases and close to grain boundaries of martensite phases was estimated with nanoindentations formed in ferrite phases and 300 nm–700 nm distant from martensite phases, such as the location in Fig. 2d. GNDs are known to form in ferrite phases by volume expansion of the martensite phase transformation because of the greater hardness of martensite than ferrite phases. GNDs are formed by martensite phase transformation inside the thickness d_{GND} from martensite phases with $d_{GND} = 0.25d_M$, where d_M is the size of the martensite phase [18]. About 1 µm of d_{GND} is estimated in DPs and CP1 steels because of its martensite phase size above 4 µm, so that the range from 700 nm is decided for a noticeable GND layer. Changes in hardness in this region at the edge of ferrite phases next to martensite phases are important since this region could be vulnerable point for formability [19]. Primary cracks may possibly be introduced in this region during HER testing since the ferrite phase is the weakest and the martensite phase the hardest in both DPs and CP1. Furthermore, strain-hardening by GNDs introduced during martensite transformation occurs mainly in this region, and thus a strain gradient is generally formed [18,19]. It is important to note that the hardness of GND layers could be strengthened by the interfacial boundaries

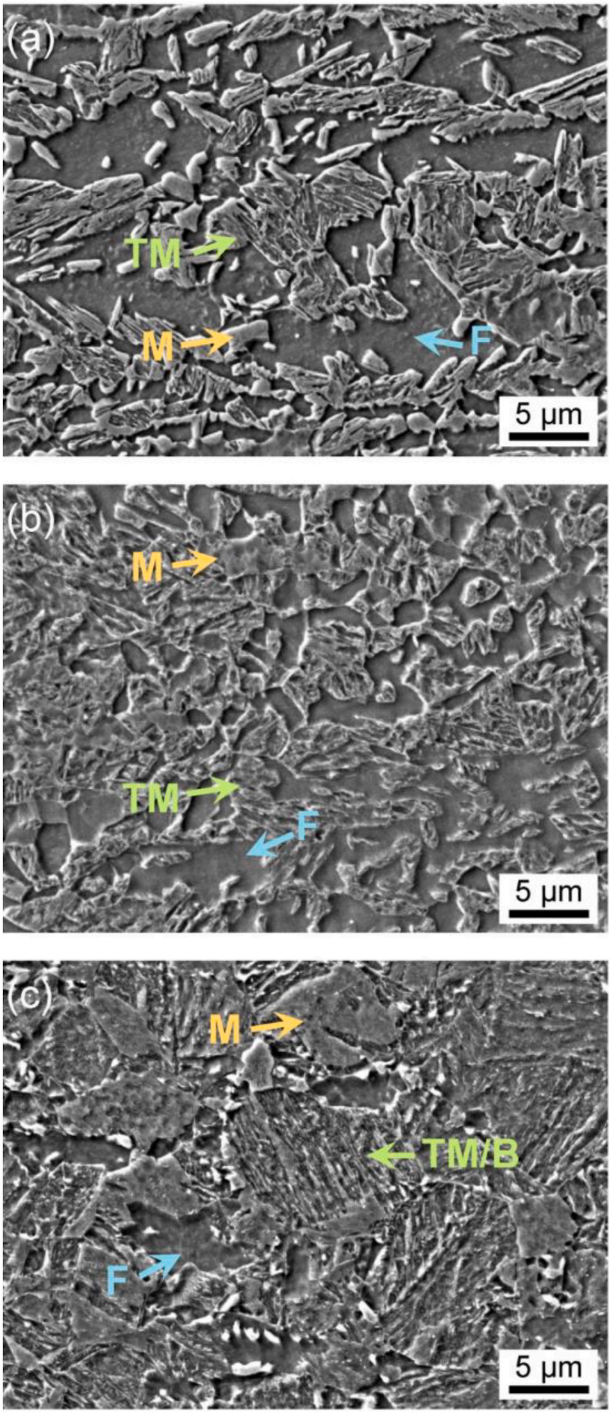

Fig. 3. SEM images showing microstructure of as-received (a) DP1, (b) DP2, and (c) CP1. Ferrite, martensite, and tempered martensite phases are indicated as F, M, and TM, respectively. For CP1, tempered martensite phases are grouped with bainite phases, which is indicated as TM/B.

Table 2

Phase volume fractions in DP1, DP2, and CP1 steels.

	Ferrite	Martensite	Tempered martensite	Bainite
DP1	37	30	33	–
DP2	27	13	60	–
CP1	14	19	67	

depending on nanoindentation location. For example, under a perfect Berkovich indenter, the plastic zone radius in elastic-perfectly-plastic materials, c, is determined as 5.9 times the indentation depth, δ [20]. With a maximum indentation depth of 100 nm and distance from grain boundaries ranging from 300 to 700 nm, some plastic zones can include grain boundaries. More than 20 nanoindentation results were analyzed for hardness of GND layers for each sample, and thus the hardness results for the GND layers are statistically comparable.

3. Results and discussion

3.1. Microstructure of DPs and CP steels

Fig. 3 shows SEM images of DP1, DP2, and CP1 prepared by electropolishing with an acetic acid-based solution, where ferrite, martensite, tempered martensite, and tempered martensite/bainite are indicated as F, M, TM, and TM/B, respectively. In the SEM images of the electropolished steel sample surfaces, ferrite (blue arrows), martensite (yellow arrows), and tempered martensite (green arrows) phases were clearly distinguishable: since the etch rate of the ferrite phase during electropolishing is greater than that of the other phases, ferrite phases appear as dented plains. Whereas the surfaces of martensite phases seem smooth, the surfaces of tempered martensite and bainite phases are made rough by cementite precipitates embedded in the matrix or dents formed by removal of the cementite precipitates during electropolishing.

Distinguishing tempered martensite and bainite phases based on the distribution of cementite precipitates in CP1 is not as clear as distinguishing ferrite, martensite, and tempered martensite phases in the

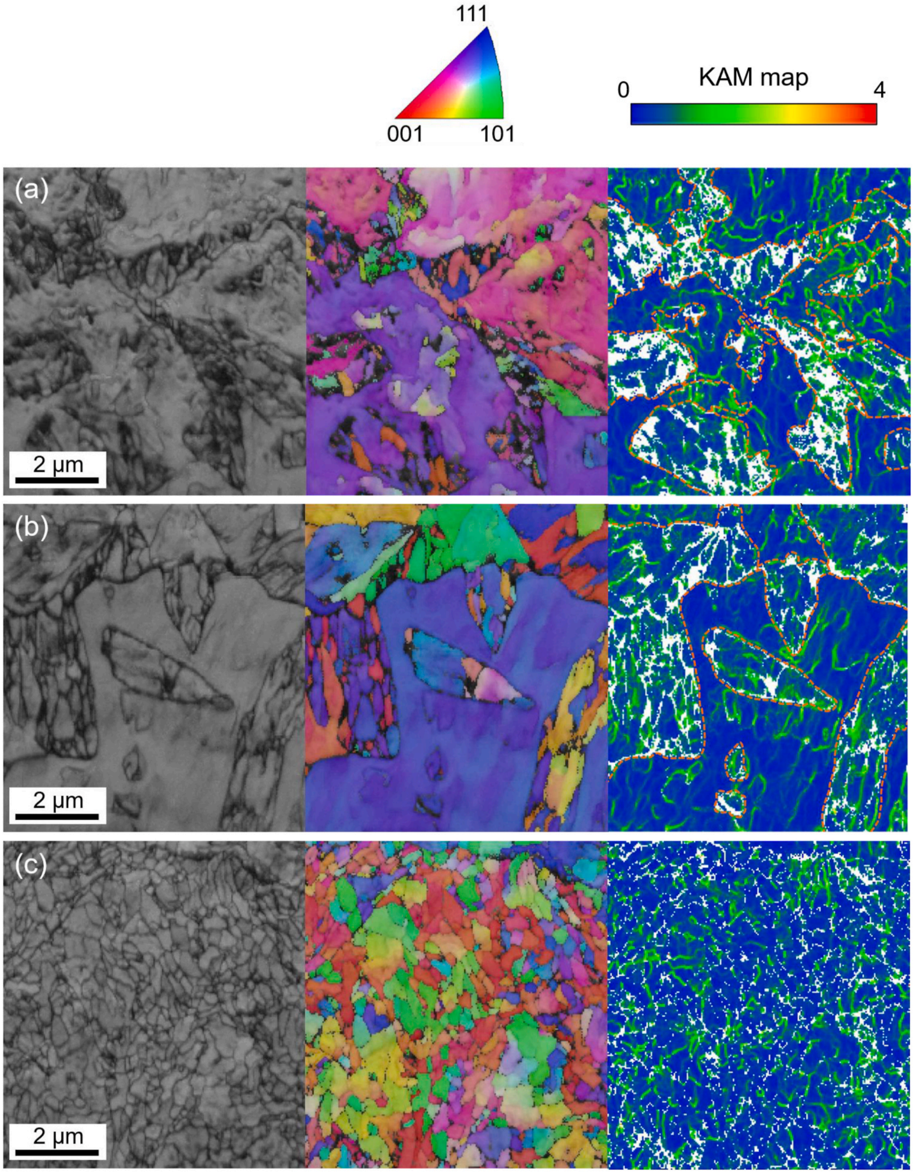

Fig. 4. EBSD analysis including band contrast, inverse pole figure, and kernel misorientation (KAM) map of (a) DP1, (b) DP2, and (c) CP1.

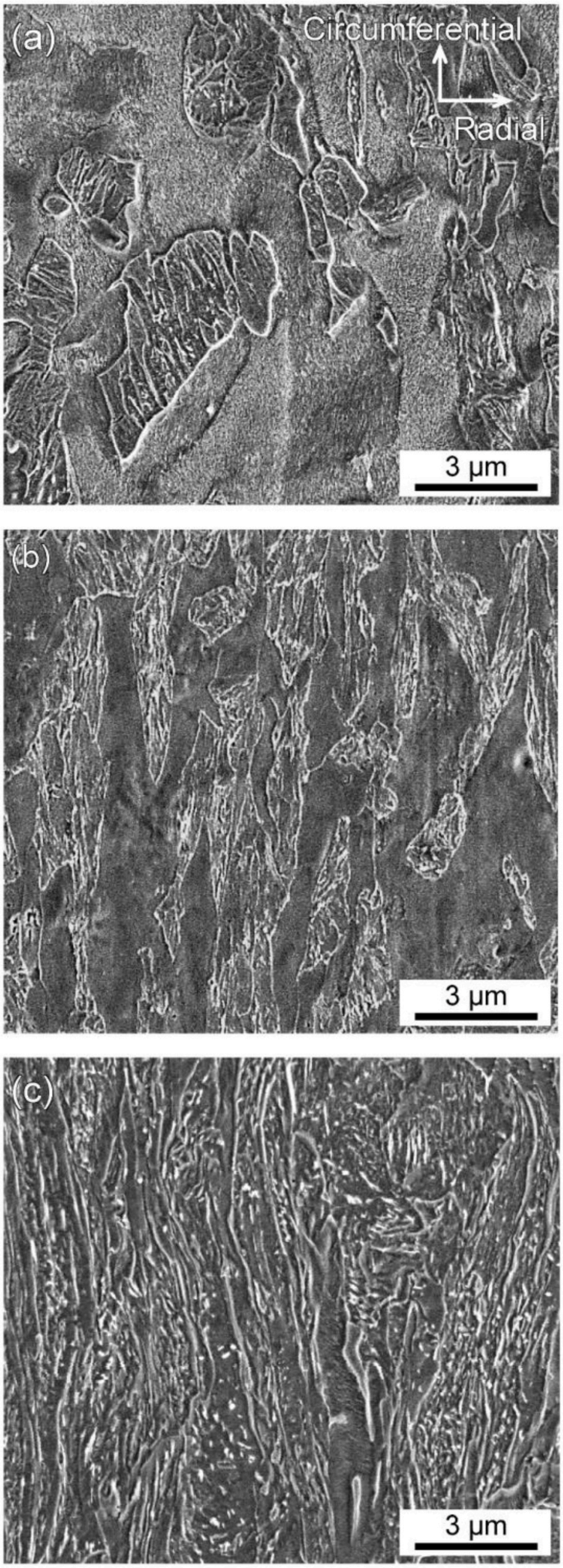

Fig. 5. SEM images showing microstructure after HER testing in (a) DP1, (b) DP2, and (c) CP1.

dual-phase steels shown in Fig. 3(a–c), so that tempered martensite and bainite phases are grouped as TM/B in CP1. Volume fractions of constituent phases in DPs and CP1 are evaluated based on SEM observations and listed in Table 2. As for DP1, all constituent phases have volume fraction close to 30%. As for DP2 and CP1, ferrite and martensite phases have volume fraction close to 20% respectively, and the other phases, including tempered martensite and bainite phases, have volume fraction greater than 50%.

Fig. 4 shows EBSD results including band contrast, inverse pole figure, and kernel average misorientation (KAM) map of DP1, DP2, and CP1 steels. A ferrite phase with BCC structure was input as reference crystal structure. For martensite phases with BCT structure, the confidence index (C.I.) in the inverse pole figure is below 0.1, which is denoted as white points in misorientation map. For tempered martensite phases with BCC structure, C.I. in the inverse pole figure is greater than 0.1, while highly dense misorientations are observed in KAM map. In DP1 and DP2, ferrite phases are distinguished from martensite and tempered martensite phases and denoted by orange dotted lines in the KAM map. Misorientations are also observed in ferrite phases surrounded by martensite and tempered martensite phases, meaning that GNDs were formed in the ferrite phase by volume expansion of the martensite phase transformation. However, in CP1, the constituent phases are indistinguishable, with a uniformly dispersed misorientation and few points with C.I. below 0.1. It seems that an appropriate tempering process for CP1 enhanced carbon diffusion in martensite and tempered martensite phases, resulting in few differences in the crystal structures of martensite, tempered martensite, bainite and ferrite phases. Nevertheless, it is obvious that misorientations by GNDs are dispersed in ferrite phases as much as in other phases.

3.2. Microstructure and void formation after HER test

Hole expansion ratio tests were performed until the final hole diameter, d_f, reaches 15.1 (±0.2) mm in DP1, 22.6 (±1.0) mm in DP2 and 23.6 (±0.5) mm in CP1. HER was calculated by HER $= \frac{d_f - d_0}{d_0} \times 100(\%)$, yielding a HER of 51.0 (±2.5)% for DP1, 126.4 (±10.0)% for DP2 and 136.2 (±5.0)% for CP1.

The SEM images in Fig. 5 of DP1, DP2, and CP1 after HER testing show typical microstructures in nanoindentation locations. The vertical and horizontal axes in these images correspond to circumferential and radial directions, respectively, in HER tests. Unlike the isotropic morphologies of constituent phases before HER tests (Fig. 3), the constituent phases except martensite phases in DP1 elongated more along the circumferential direction since the triaxial stress state introduced at the edge of the hole during HER tests applied much greater strain in the circumferential direction than in the radial and thickness directions. The unremarkable elongation of martensite in DP1 shows that deformation of DP1 is mostly accompanied by deformation of ferrite and tempered martensite phases, whereas the deformation of DP2 and CP1 seems to occur uniformly with all constituent phases.

Fig. 6 shows the size distributions of voids and SEM images showing voids observed in about 50 μm away from the edge of the hole in 51%, 126.4%, and 136.2% HER-tested DP1, DP2, and CP1 to investigate stress concentration prior to primary crack propagation. A total 100 μm × 100 μm area was observed to investigate size distribution, and typical morphologies of observed voids are indicated with arrows in Fig. 6(d–f). As a parameter of stress concentration, void size is defined as the length from the highest point to the lowest point of individual voids in a circumferential direction, because strain in the circumferential direction is much the greatest during HER testing [21]. Although elongated void morphology could contribute additional stress concentration, the greater strain in the circumferential direction has insignificant morphological effects on void size. (The size distribution of voids includes only those larger than 100 nm to avoid including other artifacts such as carbide precipitates and etched patterns. Nevertheless, we note

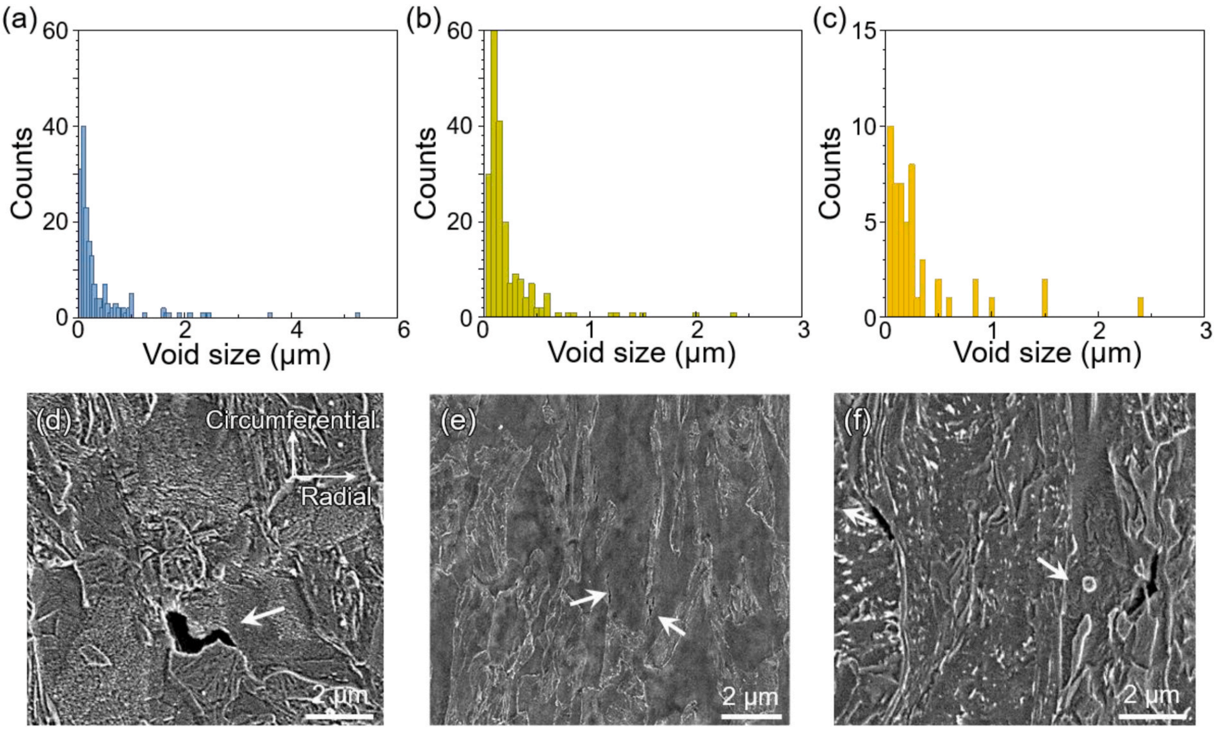

Fig. 6. (a–c) Size distributions of voids and (d–f) SEM image showing typical void formation observed after HER testing in (a, d) DP1, (b, e) DP2, and (c, f) CP1.

that there are still uncertainties in the quantitative values because the analysis was performed manually and under limited magnification.)

In DP1, the void size ranges from 100 nm to 6 μm; 79% of voids, including those larger than 3 μm, are located at interfacial boundaries (Fig. 6d) and only 3% and 18% of voids are observed inside ferrite and martensite phases. In DP2 and CP1, voids smaller than 3 μm are observed, which means lower stress concentration than in DP1. In DP2, only 38% of voids are located at interfacial boundaries between ferrite and martensite phases. The size of these voids ranges from 100 nm to 2.4 μm, most of them below 1 μm. 53% of voids are in ferrite phases along the circumferential direction (Fig. 6e). Some of these are close to interfacial boundaries next to martensite phases, where severe geometrically necessary dislocations (GNDs) could accumulate by martensite phase transformation [18], so they could be formed in GND layers. 9% of voids were observed inside martensite phases, with sizes of about 300 nm. In CP1 deformed with the greatest HER, the total number of voids observed by SEM is much lower than in DPs, and the void size in CP1 is generally smaller than in DPs. Most voids formed with elongated shape between hard phases (Fig. 6f), which are considered martensite since voids between elongated hard phases in circumferential direction have been reported to be the result of necking in the martensite phase [6, 22]. The void size ranges from 300 nm to 2.4 μm. Interfacial voids between ferrite and martensite phases were also observed, with size below 1 μm. Unlike DP1 with unremarkable elongation of martensite phases and dominant void formation at interfacial boundaries (Figs. 5a and 6d), interfaces are not the primary site of void formation in DP2 and CP1. Instead, GND layer and martensite phases seem to operate as the primary site of void formation in DP2 and CP1, also revealing the operation of GND layer and martensite phases as dominant stress concentration sites in DP2 and CP1.

3.3. *Strain hardening in individual phases and GND layer during HER testing*

Figs. 7 and 8 show hardness distributions in DP1, DP2, and CP1 before and after HER testing; Nanoindentation force-depth curves and their hardnesses corresponding to ferrite (F), martensite (M), and bainite/tempered martensite phases are shown in blue, red, and green, respectively. The average hardnesses of ferrite ($\overline{H}_F$), martensite ($\overline{H}_M$), and tempered martensite (including bainite) phases ($\overline{H}_{TM}$) are summarized in Table 3. For the initial DP1, the average hardnesses of ferrite and tempered martensite phases are much below that of martensite phases, yielding a wide hardness distribution and high hardness ratios between the hardest and the softest phases, $\overline{H}_M/\overline{H}_F$ of 2.94. For the initial DP2 and CP1, narrower hardness distributions are observed, with hardness ratio $\overline{H}_M/\overline{H}_F$ of 1.59 in DP2 and 1.63 in CP1. Hardness ratio $\overline{H}_M/\overline{H}_F$ lower than DP1 and previous reports (ranging from 1.7 to 2.6) and average martensite hardness $\overline{H}_M$ close to that of tempered martensite$\overline{H}_{TM}$, can be attributed to appropriate tempering for DP2 and CP1. For HER-tested DP1, the hardness distribution is as wide as before HER testing. Meanwhile, HER-tested DP2 and CP1 show that all constituent phases were hardened by severe deformation and the hardness distributions of constituent phases widened. Hardnesses of the GND layer were analyzed before and after HER tests, with results of 4.36 (±1.03) GPa and 5.52 (±0.99) GPa in DP1, 4.47 (±0.65) GPa and 6.03 (±1.29) GPa in DP2, and 4.36 (±0.91) GPa and 7.36 (±1.12) GPa in CP1.

Fig. 9 shows the increase in hardness of individual phases and GND layer after HER testing, which is related to the amount of strain-hardening occurring during HER testing. DP1 has a notable hardness increase only in the ferrite and tempered martensite phases; the hardness increase in martensite phases is relatively low. This is consistent with the unremarkable elongation of martensite phases and the overwhelming voids at interfacial boundary in Fig. 6d. These results showing a HER of 51% in DP1, lower than the others, is attributed to the high hardness ratio and large strain disparity, as reported in previous research [14].

In DP2 and CP1, hardness generally increases uniformly for all constituent phases including GND layer, indicating that strain was generated dispersedly overall, as also observed in Fig. 5b and c. The narrow hardness distribution of the constituent phases and the lower hardness ratio$\overline{H}_M/\overline{H}_F$ of about 1.6 are attributable to stress dispersion and enhanced HERs of DP2 and CP1. Interestingly, despite the similar

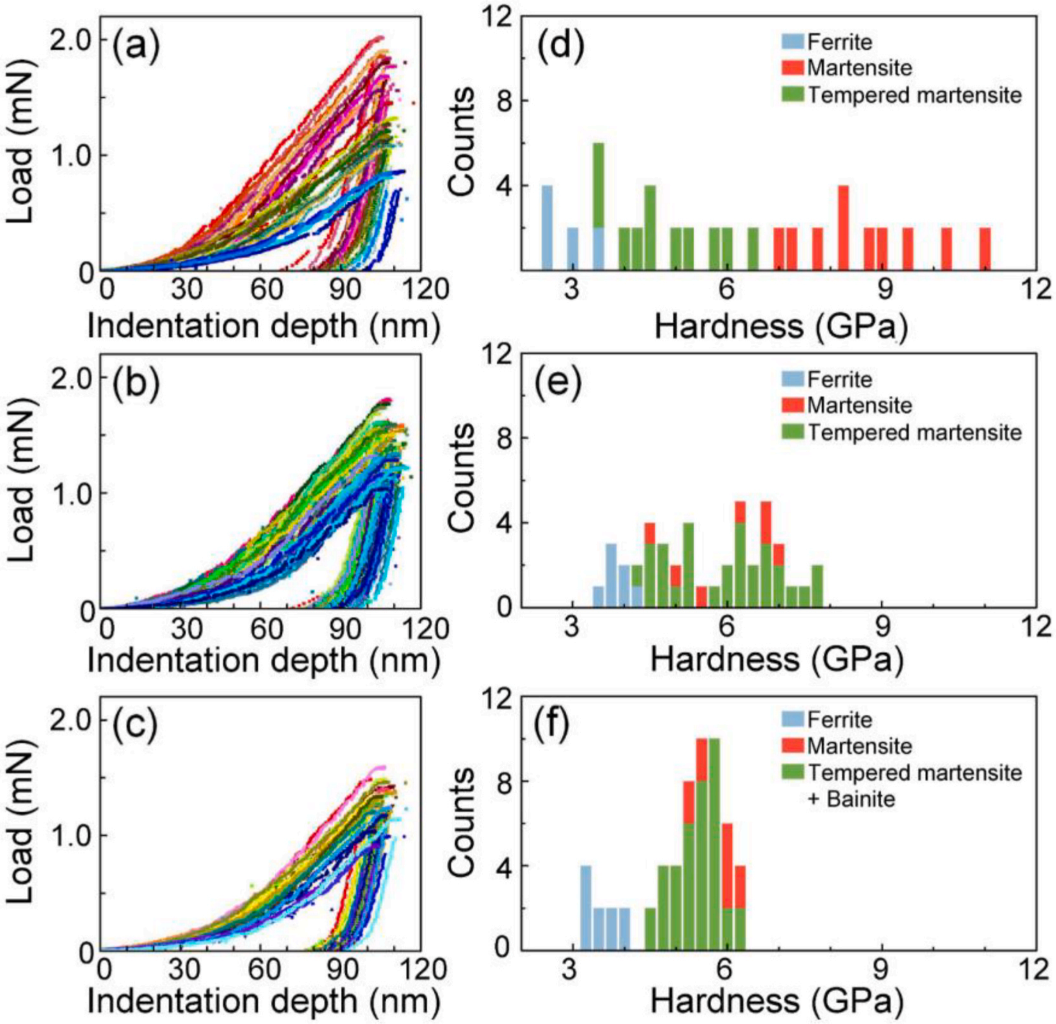

Fig. 7. Nanoindentation force-depth curves and hardness distributions of constituent phases of (a), (d) DP1, (b), (e) DP2, and (c), (f) CP1, before HER tests. Ferrite, bainite/tempered martensite, and martensite phases are indicated by shades of blue, green, and red, respectively. (For interpretation of the references to colour in this figure legend, the reader is referred to the Web version of this article.)

hardness distribution and phase volume fraction in DP2 and CP1, CP1 has 10% greater HER and lower void density than DP2. Also, the increase in hardness of the GND layers decreases in the order CP1, DP2, and DP1, which is the same order of HER and the narrowness of the hardness distributions of constituent phases.

3.4. *Influence of hardness gradient on the strain hardenability of individual phases*

A possible factor in formability is the strain-hardenability of the GND layer, which operated as a primary void formation site in DP2. Fig. 10 shows schematic diagrams (*y*-axis to scale) of hardness distributions in martensite and ferrite phases, including the GND layer for DP2 and CP1; martensite phases, GND layers, and ferrite phases, and hardness gradients at interfaces between them, indicated as zones 1 and 2. Values highlighted in yellow and blue are hardness before and after HER testing, respectively. The hardness of the GND layers in ferrite phases is greater than in the ferrite-phase interiors, by 15.8% for DP2 and 23.2% for CP1. The hardness of the GND layers has the relation $H_{GND} = 0.27$ $(H_M\text{-}H_F)$ in DP2 and $H_{GND} = 0.37(H_M\text{-}H_F)$ in CP1, where H_{GND} is the hardness of the GND layer. After HER testing, DP2 still follows the relation $H_{GND} = 0.27(H_M\text{-}H_F)$, while CP1 follows the relation $H_{GND} =$ $0.33(H_M\text{-}H_F)$, which has a still steeper hardness gradient in zone 2 as well as larger average hardness than DP2. That is, greater deformation of ferrite phases in CP1 accompanied the greater deformation of the GND layer, without numerous voids that could enhance strain distribution over the ferrite phases [19].

This greater deformation of the GND layer can result from the initial hardness gradient from martensite phase to GND layer (zone 1) and from the GND layer to the interior of ferrite phase (zone 2). DP2 has a steeper hardness gradient in zone 1 than in zone 2, meaning that the stress concentration is higher in zone 1 than zone 2. As deformation proceeds, the strain in the GND layer is localized in zone 1 and the hardness gradient in zone 1 becomes much greater than in zone 2. This increasing stress gradient could cause the stress concentration at GND layer and the numerous voids below 1 μm formed in the GND layers. Accordingly, it seems that strain-hardening of the GND layer is reduced by the increasing stress concentration at the GND layer as deformation proceeds.

Meanwhile, CP1 shows a smaller difference in hardness gradient in zones 1 and 2 than DP2, meaning that the stress concentration in zone 1 is less than in DP2. As a result, the GND layer could deform and harden as much as the interior of ferrite phases deforms, and strain distribution could be sustained during HER testing. Simultaneously, it is possible that dense GNDs surrounding ferrite phase boundaries suppress dislocation motion from the interior of ferrite phases to phase boundaries, which is called back stress [23]. An increasing back stress with increasing GND layer hardness could also be a factor enhancing uniform deformation of

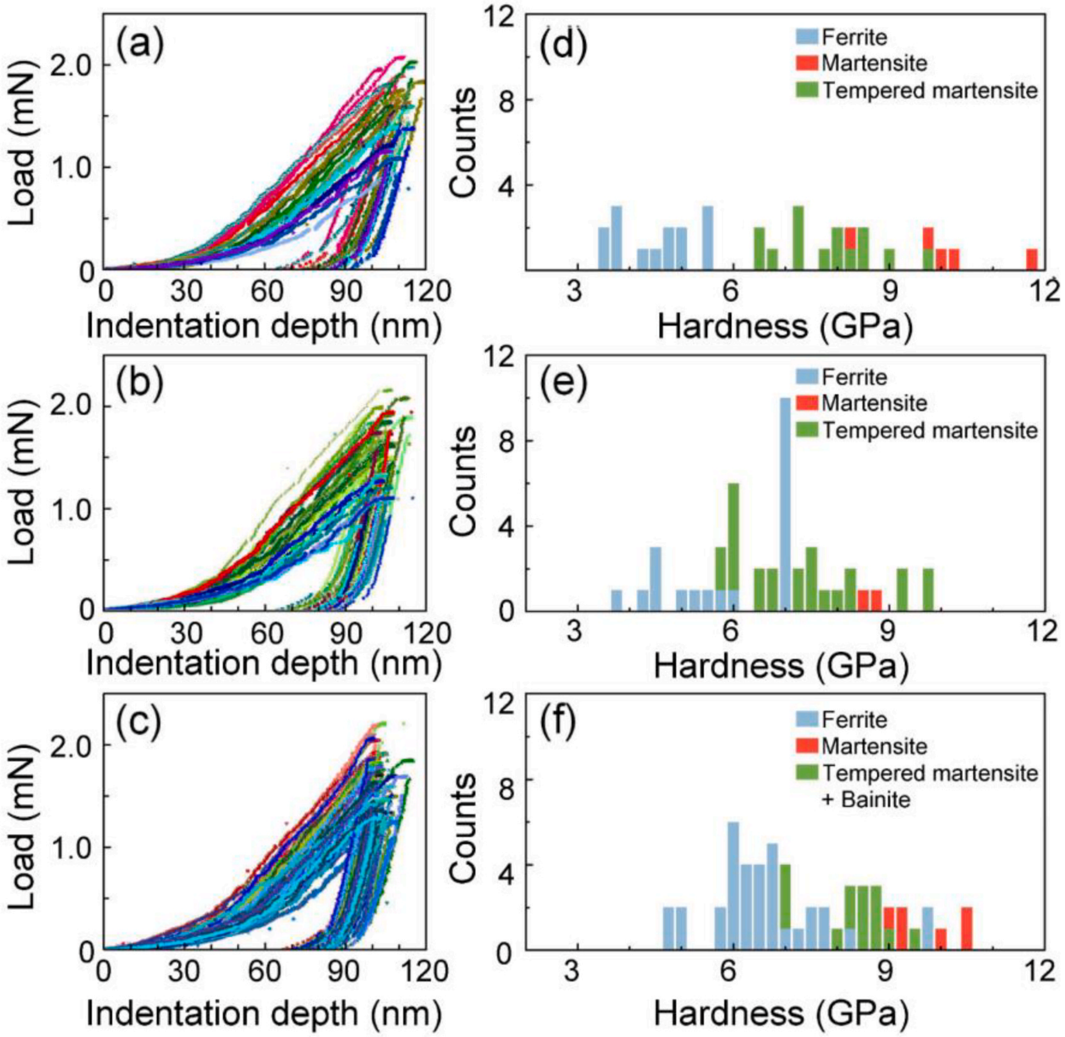

Fig. 8. Nanoindentation force-depth curves and hardness distributions of constiutent phases of (a), (d) DP1, (b), (e) DP2, and (c), (f) CP1, after HER tests. Ferrite, bainite/tempered martensite, and martensite phases are indicated by shades of blue, green, and red, respectively. (For interpretation of the references to colour in this figure legend, the reader is referred to the Web version of this article.)

Table 3
Hardnesses (GPa) of ferrite, martensite, and tempered martensite (including bainite in case of CP1) phases before and after HER tests.

As-received sample	Ferrite ($\overline{H}_F$)	Martensite ($\overline{H}_M$)	Tempered martensite ($\overline{H}_{TM}$)	$\overline{H}_M/\overline{H}_F$
DP1	2.96 (±0.50)	8.69 (±1.30)	4.82 (±0.93)	2.94
DP2	3.86 (±0.22)	6.15 (±1.00)	5.96 (±1.04)	1.59
CP1	3.54 (±0.34)	5.76 (±0.39)	5.53 (±0.70)	1.63
HER-tested sample	**Ferrite ($\overline{H}_F$)**	**Martensite ($\overline{H}_M$)**	**Tempered martensite ($\overline{H}_{TM}$)**	**$\overline{H}_M/\overline{H}_F$**
DP1	4.49 (±0.76)	9.57 (±0.87)	8.14 (±1.52)	2.13
DP2	5.08 (±0.92)	8.63 (±0.05)	7.57 (±1.47)	1.70
CP1	6.60 (±1.12)	8.91 (±1.05)	7.77 (±1.01)	1.35

ferrite phases, including the GND layer.

These results suggest that the hard GND layers relative to ferrite phases may play the role of stress dispersion layers in void formation when DP2 and CP1 have enhanced HER values by a low hardness ratio between hard and soft phases in this study. If hardness of the GND layer is close to that of the ferrite phases, stress concentrates more at interfacial boundaries between ferrite and martensite phases. If the hardness of the GND layers is similar to the average hardness of the martensite and ferrite phases, GND layers may play a role in dispersing stress concentrations at interfacial boundaries and could show enhanced strain-hardenability comparable to ferrite phases, resulting in the enhancement of formability.

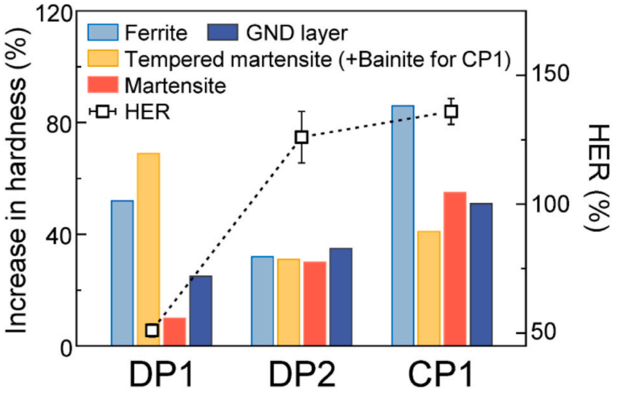

Fig. 9. Increase in hardness of constituent phases after HER tests and HER values.

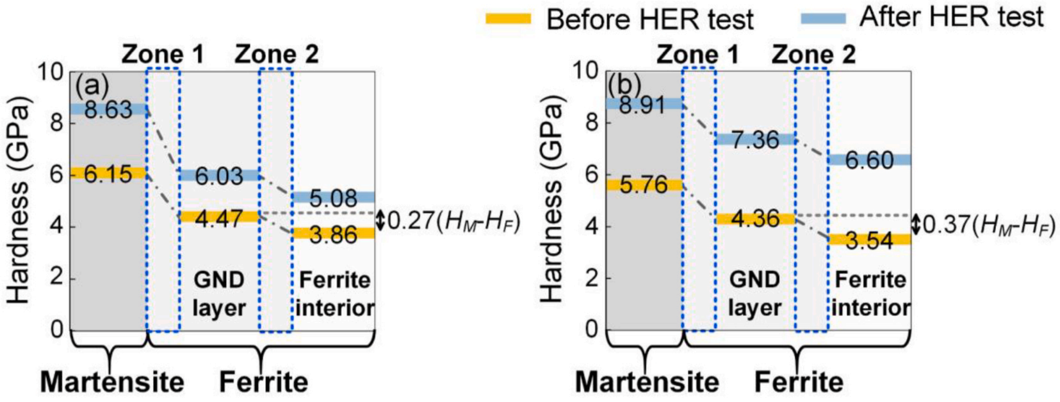

Fig. 10. Schematic of hardness distribution along with martensite phase, GND layer in ferrite phase, and ferrite interior with real scale of y-axis in (a) DP2 and (b) CP1.

4. Conclusions

This study investigates the dependence of strain hardenability of constituent phases on the hardness of GND layer as well as hardness ratio at interfacial boundaries and the correlation of those properties with formability in dual and complex-phase steels. DP and CP steels with diverse hardness distributions were prepared by tempering processes. Formability of the DP and CP steels was measured by HER tests and the hardness of constituent phases was measured by nanoindentations before and after the HER tests. In DP1, HER of 51% was measured and interfacial void formation was dominantly observed, which was attributed to the high hardness ratio between the ferrite and martensite phases. In DP2 and CP1, with low hardness ratio between ferrite and martensite phases, interfacial void formation is suppressed and HER of 126.4% and 136.2% were measured. In DP2, many voids were observed in the GND layers and at the interfacial boundaries, which was attributable to the high hardness gradient in zone 1. In CP1, many fewer voids than in the DPs were observed, and greater strain hardening were generated in GND layer. These results were attributed to the intermediate hardness of the GND layers relative to that of the martensite and ferrite phases. Since the GND layers operate as stress-dispersion layers, stress concentration and strain disparity near interfacial boundaries were alleviated.

CRediT authorship contribution statement

Eunji Song: Methodology, Validation, Investigation, Writing – original draft, Writing – review & editing. **Gun-Hee Lee:** Methodology, Data curation. **Hansol Jeon:** Validation, Investigation. **Bong June Park:** Conceptualization, Writing – original draft, Supervision. **Jung-Gu Lee:** Conceptualization, S, Writing – original draft, Supervision. **Ju-Young Kim:** Conceptualization, Writing – original draft, Writing – review & editing, Supervision.

Declaration of competing interest

The authors declare that they have no known competing financial interests or personal relationships that could have appeared to influence the work reported in this paper.

Acknowledgments

This work was supported by the National Research Foundation of Korea (NRF) grants funded by the Ministry of Science and ICT (MSIT) (2020R1A5A6017701 and 2020R1F1A1076140).

References

[1] M. Sudo, T. Iwai, Deformation behavior and mechanical properties of ferrite-bainite-martensite (triphase) steel, Trans. ISIJ 23 (1983) 294–302.

[2] H. Ghadbeigi, C. Pinna, S. Celotto, J.R. Yates, Local plastic strain evolution in a high strength dual-phase steel, Mater. Sci. Eng., A 527 (2010) 5026–5032.

[3] C.C. Tasan, J.P.M. Hoefnagels, M. Diehl, D. Yan, F. Roters, D. Raabe, Strain localization and damage in dual phase steels investigated by coupled in-situ deformation experiments and crystal plasticity simulations, Int. J. Plast. 63 (2014) 198–210.

[4] K. Park, M. Nishiyama, N. Nakada, T. Tsuchiyama, Effect of the martensite distribution on the strain hardening and ductile fracture behaviors in dual-phase steel, Mater. Sci. Eng., A 604 (2014) 135–141.

[5] J. Kadkhodapour, A. Butz, S. Ziaei Rad, Mechanisms of void formation during tensile testing in a commercial, dual-phase steel, Acta Mater. 59 (2011) 2575–2588.

[6] M. Azuma, S. Goutianos, N. Hansen, G. Winther, X. Huang, Effect of hardness of martensite and ferrite on void formation in dual phase steel, Mater. Sci. Technol. 28 (2012) 1092–1100.

[7] C. Landron, O. Bouaziz, E. Maire, J. Adrien, Characterization and modeling of void nucleation by interface decohesion in dual phase steels, Scripta Mater. 63 (2010) 973–976.

[8] G. Cheng, F. Zhang, A. Ruimi, D.P. Field, X. Sun, Quantifying the effects of tempering on individual phase properties of DP980 steel with nanoindentation, Mater. Sci. Eng., A 667 (2016) 240–249.

[9] Y. Choi, W.Y. Choo, D. Kwon, Analysis of mechanical property distribution in multiphase ultra-fine-grained steels by nanoindentation, Scripta Mater. 45 (2001) 1401–1406.

[10] C. Du, F. Maresca, M.G.D. Geers, J.P.M. Hoefnagels, Ferrite slip system activation investigated by uniaxial micro-tensile tests and simulations, Acta Mater. 146 (2018) 314–327.

[11] J.L. Stewart, L. Jiang, J.J. Williams, N. Chawla, Prediction of bulk tensile behavior of dual phase stainless steels using constituent behavior from micropillar compression experiments, Mater. Sci. Eng., A 534 (2012) 220–227.

[12] M.Y. Seok, Y.J. Kim, I.C. Choi, Y. Zhao, J.I. Jang, Predicting flow curves of two-phase steels from spherical nanoindentation data of constituent phases: isostrain method vs. non-isostrain method, Int. J. Plast. 59 (2014) 108–118.

[13] B.W. Choi, D.H. Seo, J.Y. Yoo, J.I. Jang, Predicting macroscopic plastic flow of high-performance, dual-phase steel through spherical nanoindentation on each microphase, J. Mater. Res. 24 (2009) 816–822.

[14] M.D. Taylor, K.S. Choi, X. Sun, D.K. Matlock, C.E. Packard, L. Xu, F. Barlat, Correlations between nanoindentation hardness and macroscopic mechanical properties in DP980 steels, Mater. Sci. Eng., A 597 (2014) 431–439.

[15] P. Huyghe, S. Depinoy, M. Caruso, D. Mercier, C. Georges, L. Malet, S. Godet, On the effect of Q&P processing on the stretch-flange-formability of 0.2C ultra-high strength steel sheets, ISIJ Int. 58 (2018) 1341–1350.

[16] N. Pathak, C. Butcher, M.J. Worswick, E. Bellhouse, J. Gao, Damage evolution in complex-phase and dual-phase steels during edge stretching, Materials 10 (2017) 346.

[17] K. Hasegawa, K. Kawamura, T. Urabe, Y. Hosoya, Effects of Microstructure on Stretch-flange-formability of 980MPa Grade cold-rolled ultra high strength steel sheets, ISIJ Int. 44 (2004) 603–609.

[18] A. Ramazani, K. Mukherjee, A. Schwedt, P. Goravanchi, U. Prahl, W. Bleck, Quantification of the effect of transformation-induced geometrically necessary dislocations on the flow-curve modelling of dual-phase steels, Int. J. Plast. 43 (2013) 128–152.

[19] H. Ghassemi-Armaki, R. Maab, S.P. Bhat, S. Sriram, J.R. Greer, K.S. Kumar, Deformation response of ferrite and martensite in a dual-phase steel, Acta Mater. 62 (2014) 197–211.

[20] M. Delince, T.J. Pardoen, Separation of size-dependent strengthening contributions in fine-grained dual phase steels by nanoindentation, Acta Mater. 54 (2006) 3395–3404.

[21] J.H. Kim, M.G. Le, D. Kim, D.K. Matlock, R.H. Wagoner, Hole-expansion formability of dual-phase steels using representative volume element approach with boundary-smoothing technique, Mater. Sci. Eng., A 527 (2010) 7353–7363.

[22] J. Kadkhodapour, A. Butz, S. Ziaei-Rad, S. Schmauder, A micro mechanical study on failure initiation of dual phase steels under tension using single crystal plasticity model, Int. J. Plast. 27 (2011) 1103–1125.

[23] H.K. Park, K. Ameyama, J. Yoo, H. Hwang, H.S. Kim, Additional hardening in harmonic structured materials by strain partitioning and back stress, Mater. Res. Lett. 6 (2018) 261–267.